RSC Advances

PAPER

View Article Online
View Journal | View Issue

Cite this: *RSC Adv.*, 2023, **13**, 10657

Study on the photocatalytic properties differences between the 1-D and 3-D $W_{18}O_{49}$ particles†

Juan Wang, *[a] Zhaoxiang Wang,[a] Jichao Gao[a] and Jin Ye*[b]

The morphology of $W_{18}O_{49}$ catalysts has a significant effect on their photocatalytic performance. Herein, we successfully prepared two commonly used $W_{18}O_{49}$ photocatalysts just by changing the reaction temperature in the hydrothermal system, namely 1-D $W_{18}O_{49}$ nanowires (1-D $W_{18}O_{49}$) and 3-D urchin-like $W_{18}O_{49}$ particles (3-D $W_{18}O_{49}$), and evaluated the difference of their photocatalytic performances by taking the degradation of methylene blue (MB) as an example. Remarkably, 3-D $W_{18}O_{49}$ exhibited an impressive photocatalytic degradation performance towards MB with photocatalytic reaction rates of 0.00932 min^{-1}, which was about 3 times higher than that of 1-D $W_{18}O_{49}$. The comprehensive characterization and control experiments could further reveal that the hierarchical structure of 3-D $W_{18}O_{49}$ brought higher BET surface areas, stronger light harvesting, faster separation of photogenerated charges and so on, which was the main reason for its better photocatalytic performance. ESR results confirmed that the main active substances were superoxide radicals ($^{\bullet}O_2^-$) and hydroxyl radicals ($^{\bullet}OH$). This work aims to explore the intrinsic relationship between the morphology and photocatalytic properties of $W_{18}O_{49}$ catalysts, so as to provide a theoretical basis in the morphology selection of $W_{18}O_{49}$ or its composite materials in the field of photocatalysis.

Received 15th February 2023
Accepted 27th March 2023

DOI: 10.1039/d3ra01031g

rsc.li/rsc-advances

1 Introduction

With the advent of environmental matters and the energy crisis, the oxide semiconductor photo-catalysts have received extensive attention and research given that their energy source is renewable solar energy.[1,2] Among various transition metal oxides, earth-abundant tungsten oxides have been proved to be ideal candidates for photocatalytic systems, attributed to their chemical stability, wide bandgap and strong adsorption of the solar spectrum.[3,4] Tungsten mainly has three stoichiometric oxides: WO_2, W_2O_5 and WO_3, of which WO_3 is the most commonly used due to its high sensitivity. In the actual preparation process of WO_3, part of the tungsten is reduced to form non-stoichiometric tungsten oxide (WO_{3-x}, $0 \leq x \leq 1$) with mixed valence states of +6 and +5, such as $WO_{2.90}$ ($W_{20}O_{58}$), $WO_{2.83}$ ($W_{24}O_{68}$), $WO_{2.80}$ (W_5O_{14}), $WO_{2.72}$ ($W_{18}O_{49}$), *etc.*[5,6] In particular, the non-stoichiometric $W_{18}O_{49}$ structure is rich in more oxygen vacancies and W^{5+} defects as reaction sites to stimulate adsorption and activation of oxygen molecules, hence $W_{18}O_{49}$ has incomparable catalytic properties and novel properties for photocatalytic degradation of organic dyes, especially monoclinic phase $W_{18}O_{49}$.[7] To promote the application of $W_{18}O_{49}$ with excellent properties in more fields, more and more preparation methods have been developed to date, mainly including chemical vapor deposition, sputtering technique, micro-emulsion method, sol–gel method and hydrothermal method.[8–12] Among them, hydrothermal route exhibits the most feasibility and research value because of its easy operation, mild conditions, and more importantly, better control on the morphology of prepared particles. It is concluded by reviewing many literature that the photocatalytic efficiency of the materials mainly depends on the surface area, bandgap, crystallinity and so on, and most of these factors are closely related to the morphology of particles.[13] Therefore, it is very important to control the $W_{18}O_{49}$ particle morphology by exploring different reaction conditions in hydrothermal method. And it is more important to study the internal relationship between particle morphology and performance, so as to provide theoretical guidance for selecting suitable particle morphology in different application fields.

At present, water pollution has become an urgent global problem in current environmental matters and energy crisis, especially, the pollution from textile industries would endanger peoples life and affect aquatic life as well from remote antiquity.[14–18] Furthermore, methylene blue (MB) is one of the most commonly used organic dyes in the textile industry and is said to be composed of various aromatic amine groups, which can cause serious skin damage, cancerization and respiratory

[a]*School of Chemistry & Chemical Engineering, Linyi University, Linyi 276000, P. R. China. E-mail: juanwang117@163.com; wzx13864176731@163.com; lyly1901@126.com*

[b]*Key Laboratory of Forest Plant Ecology, Ministry of Education, College of Chemistry, Chemical Engineering and Resource Utilization, Northeast Forestry University, Harbin 150040, P. R. China. E-mail: yejin@nefu.edu.cn*

† Electronic supplementary information (ESI) available. See DOI: https://doi.org/10.1039/d3ra01031g

disease.[13,19,20] Therefore, finding the effective way to remove organic dyes from wastewater has become the top priority in environmental protection and has attracted wide attention. To better solve the above problems, more and more approaches have been carried out to degrade organic dyes, such as physical absorption, solvent extraction, biodegradation, and photocatalytic oxidation.[21–26] Among these methods, photocatalytic degradation, which utilizes semiconductor and light to solve organic dyes, is undoubtedly the most promising one by virtue of its environmental protection, high efficiency and advanced oxidation in sewage disposal.[27–29]

Having said all of the foregoing, it is very necessary to use tungsten oxide material with many superior photocatalytic performance advantages to photodegrade organic dyes. In addition, given that the morphology of $W_{18}O_{49}$ particles has a big influence on its photocatalytic properties, various morphologies of $W_{18}O_{49}$ have been synthesized and tested for their photocatalytic activities. Among the available $W_{18}O_{49}$ materials, one dimensional (1-D) nanowires and three dimensional (3-D) urchin-like particles are the most desirable and excellent in the field of photocatalysis because of their uniform form and numerous performance advantages.[30–34] However, most researchers concentrate solely on investigating the properties of individual materials and their composites, and few deeply study their difference in photocatalytic properties and the fundamental reasons for such differences. The absence of this part of research content is not conducive to our better understanding of the relationship between the structure and properties for $W_{18}O_{49}$ particle and better application of them in more fields.

With the aim of understanding the effect of morphology on the photocatalytic properties of $W_{18}O_{49}$ particles, 1-D $W_{18}O_{49}$ nanowires and 3-D urchin-like $W_{18}O_{49}$ were first prepared by simply adjusting the reaction temperature in a hydrothermal system, and further taken the degradation of methylene blue as a typical example to explore the catalytic degradation efficiency of two kinds of particles. As a result, within the specified degradation time of 120 minutes, the degradation rate of 3-D urchin-like $W_{18}O_{49}$ was approximately 3 times than that of 1-D nanowires. Through the analysis of the physical and chemical properties of the two materials, it was concluded that the better catalytic performance of 3-D particles was mainly due to the existence of three-dimensional hierarchical structure with larger specific surface area, which could facilitate the visible light absorption, improve the transfer and separation of electron–hole pairs and enriche the surface electrons at the rod top owing to the multiple light scattering and directional electron transfer induced by the nanotip effect.

2 Experimental section

2.1 Materials

Tungsten(VI) chloride (WCl_6, 99.9%) and ethanol were obtained from Tianjin Kemiou Chemical Reagent Co., Ltd. Sodium sulfate (Na_2SO_4) was purchased from Tianjin Institute of Chemical Agents. All the reagents were of analytical grade and were used without any further purification.

2.2 Characterization of the as-prepared samples

The field-emission scanning electron microscope (SEM, Nano 450, FEI, USA, operated at 10 kV) and transmission electron microscopy (TEM, Talos F200S, FEI, USA, operated at 80 kV) were used to analyze the particle morphology. Energy-disperse X-ray (EDS) was carried out on a field emission scanning electron microscope (Talos F200S) to analyze elemental features of the samples. N_2 adsorption–desorption isotherm measurements were used to study the particle specific surface areas using the BET method. The crystallographic properties of the catalysts were analyzed by the X-ray powder diffractometer (Shimadzu XRD-7000). X-ray photoelectron spectroscopy was obtained at PHI-5400 (America PE) 250 xi system. The UV-Vis diffuse reflectance spectra (UV-Vis-DRS) were measured on UV-2550 UV-Vis Spectrophotometer. Photoluminescence (PL) spectroscopy was taken down by an Agilent Cary Eclipse (F-7000) at room temperature. Time-resolved photoluminescence (TRPL) spectra were investigated *via* a FLS920 fluorescence spectrometer (Edinburgh Analytical Instruments, UK). The X-ray photoelectron spectroscopy (XPS, Kratos Axis Ultra) was used to analyze the chemical composition and element valence. The electron spin resonance (EPR) spectra were recorded *via* a Bruker ELEXSYS-II E500 CW-EPR. All electrochemical and photoelectrochemical characterizations were carried out through an electrochemical workstation (CHI760E), a three-electrode system (pH 7.0) was adopted, Pt was the counter electrode, Ag/AgCl as the reference electrode, and ITO as the working electrode under visible light. Transient photocurrent response measurements were researched on an electrochemical workstation, the whole process was in the saturated solution of Na_2SO_4 (0.5 M) under visible light by controlling the light on and off. The electrochemical workstation in Nafion solution was used to test the Electrochemical impedance spectroscopy (EIS).

2.3 Preparation of 1-D $W_{18}O_{49}$ nanowires

Similar to the synthetic route previously reported.[35] In a typical recipe, 0.5 g WCl_6 was dissolved in 100 mL absolute ethanol, a clear yellow solution appeared. Then, above yellow solution was poured to a Teflon-lined autoclave and heated at 180 °C for 24 h. A blue flocculent precipitate was formed, purified several times with absolute distilled water and anhydrous ethanol, and vacuum dried at 50 °C.

2.4 Preparation of 3-D urchin-like $W_{18}O_{49}$

Refer to the synthesis route reported earlier.[36] In this process, 0.5 g W^{6+} WCl_6 was dissolved in 100 mL absolute ethanol, a clear yellow solution was formed. Then, above yellow solution was poured to a Teflon-lined autoclave and heated at 200 °C for 24 h. A blue flocculent precipitate was formed, purified several times with absolute distilled water and anhydrous ethanol, and vacuum dried at 50 °C.

2.5 Photocatalyst activity evaluation

20 mg of as-prepared photocatalysts were suspended in 50 mL of aqueous solution of MB (10 mg L^{-1}). Under visible light (400–

800 nm) with 300 W Xenon lamp, the photocatalytic degradation of MB experiments was conducted after adsorption/desorption equilibrium (1 h). Photodegradation of MB experiments was investigated by UV-Vis spectrophotometer at 664 nm.

3 Results and discussions

3.1 Morphology and composition characterizations

At first, the morphology, microstructure and elemental composition of as-prepared $W_{18}O_{49}$ materials under different reaction temperature were systematically characterized through SEM, TEM and the corresponding EDS element-mapping images. As shown in Fig. 1a–c, the obtained particles at a reaction temperature 180 °C were uniform 1-D nanowires with a diameter of about 10 nm. While, Fig. 1d and e showed the typical SEM images of the $W_{18}O_{49}$ particles with a diameter of about 496 nm obtained at 200 °C, which indicated that these particles had a layered structure consisting of central microsphere and a large number of radial nanowires. Interestingly, through the information of above SEM and TEM images in Fig. 1f, it could be seen that some nanowires on the surface of different urchin-like particles were linked to each other, resulting in the formation of 3D network nanowires. The results of high-resolution TEM images for both particles (the inserts of Fig. 1c and f) verified that the ordered lattice fringes with a spacing of 3.8 Å, which could be attributed to the (010) plane of monoclinic $W_{18}O_{49}$. These information indicated that the 1-D $W_{18}O_{49}$ nanowires and 3-D $W_{18}O_{49}$ both grew along the [010] direction. For 3-D $W_{18}O_{49}$ particles, the EDS element-mapping images of O and W were shown in Fig. 1h and i, respectively, and we could directly observe the uniform distribution of the two elements. In addition, the tungsten content in the 3-D $W_{18}O_{49}$ was 86 wt%, as shown in Fig. S1.† These results confirmed that 1-D $W_{18}O_{49}$ nanowires and 3-D $W_{18}O_{49}$ could be successfully prepared by simply adjusting the reaction temperature in a hydrothermal system, the corresponding schematic diagram was as shown in Fig. S2.† In the hydrothermal system, the $W_{18}O_{49}$ molecules growed mainly along the (010) direction, and further formed $(WO_n)^-$ particles. The particle with negative charges generated faster at 200 °C than at 180 °C, the surface tension and surface energy of the system would further increase, and the particles generated at 200 °C were more likely to gather to three-dimensional $W_{18}O_{49}$ particles under the principle that the system energy could tend to be kept to a minimum.[37] In addition, the direct result of morphological difference was that these two kinds of $W_{18}O_{49}$ materials display different BET surface areas based on the adsorption and desorption of N_2, and the corresponding results were shown in Fig. 2. The 3-D $W_{18}O_{49}$ particles had a larger specific surface area (120 $m^2\ g^{-1}$) than 1-D $W_{18}O_{49}$ nanowires (75 $m^2\ g^{-1}$) due to the existence of hierarchical structure.

Then, the crystal structure and phase composition of 1-D $W_{18}O_{49}$ and 3-D $W_{18}O_{49}$ were exhibited in Fig. 3 by XRD patterns with scanning range from 10° to 80°. And the result (Fig. 3a)

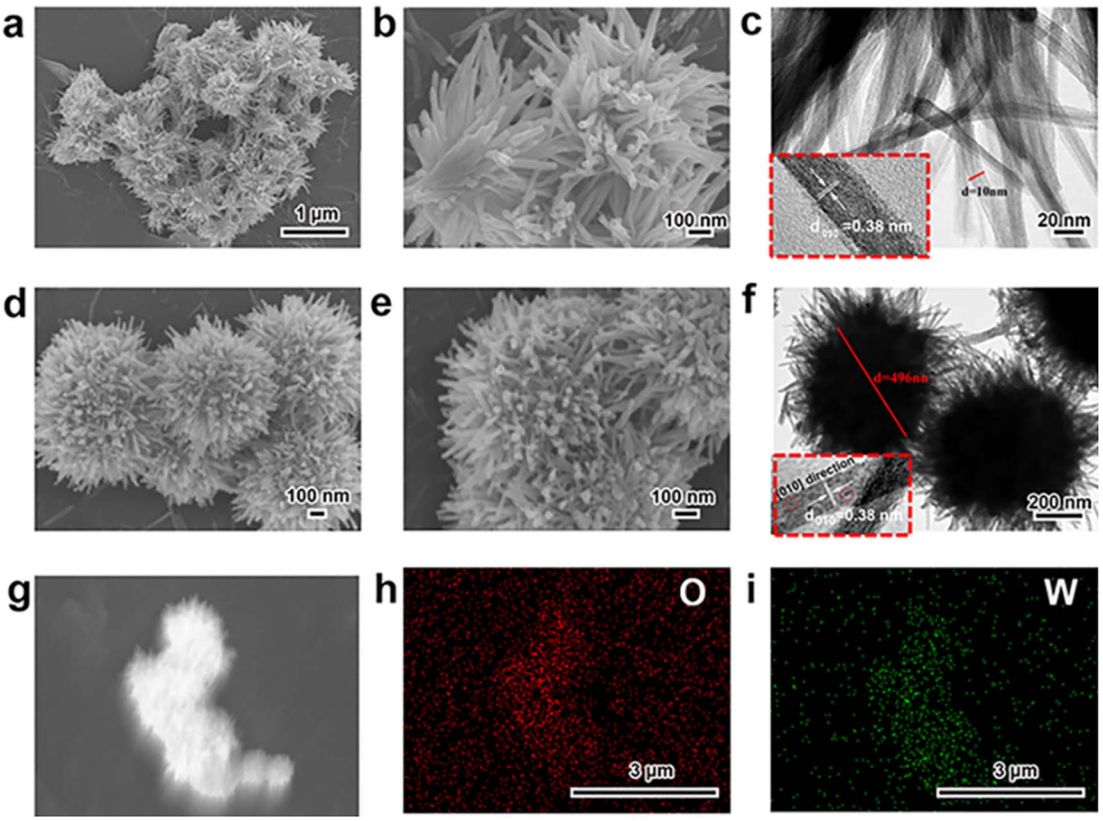

Fig. 1 SEM and TEM images of (a, b, c) 1-D $W_{18}O_{49}$ nanowires, (d, e, f) 3-D urchin-like $W_{18}O_{49}$, and (g, h, i) the EDS mapping of the elements O, W in 3-D urchin-like $W_{18}O_{49}$.

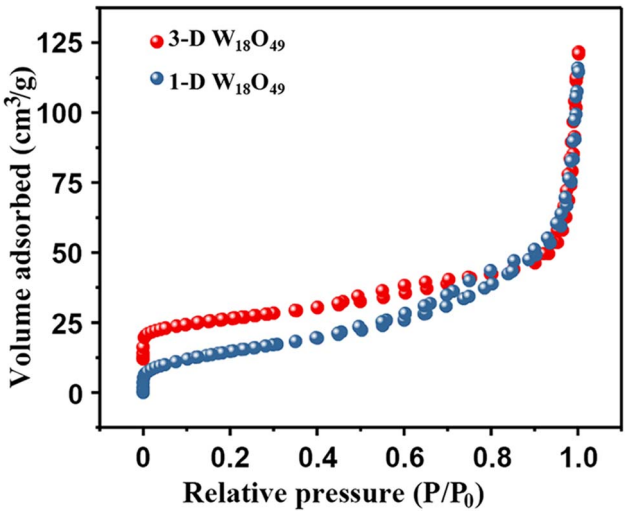

Fig. 2 Nitrogen adsorption–desorption isotherms of 1-D $W_{18}O_{49}$ nanowires and 3-D urchin-like $W_{18}O_{49}$.

showed that the position and relative intensity of the characteristic peaks of two as-prepared $W_{18}O_{49}$ samples were highly consistent with the monoclinic crystals according to the JCPDS card (no. 71-2450).[38] Specifically, the narrow and pointed peak at 23.2° matched with the (010) plane, and the weak reflection at 47.5° was in accordance with the (020) plane. Moreover, the diffraction intensities of other peaks were so weak as to be negligible. In addition, the peaks in XRD were slightly out of position with standard cards, which was due to a large number of oxygen vacancies in two sample.[39,40] Thus, the crystals of two $W_{18}O_{49}$ samples both preferentially tended to grow in (010) direction based on XRD results, which cohered with the TEM results in Fig. 1.

The detailed chemical states and chemical components of obtaining $W_{18}O_{49}$ samples were further analyzed by XPS spectra, the results were displayed in Fig. 3b–d. For accuracy, the binding energy for all the results had been corrected by C1s peak at 284.8 eV. First, the elements W, O in the 1-D $W_{18}O_{49}$ and 3-D $W_{18}O_{49}$ could be confirmed by the scanning survey spectra in Fig. 3b, and this result was in accordance with EDS mapping results (Fig. 1h and i). Moreover, the oxygen vacancies of 1-D and 3-D $W_{18}O_{49}$ were further detected by high-resolution XPS spectra of O1s (Fig. 3c), and O1s spectra of two samples were both divided into two main peaks. One peak located at 530.2 eV corresponded to the lattice oxygen of W–O, while the other one located at 531.2 eV was assigned to the oxygen vacancy. This

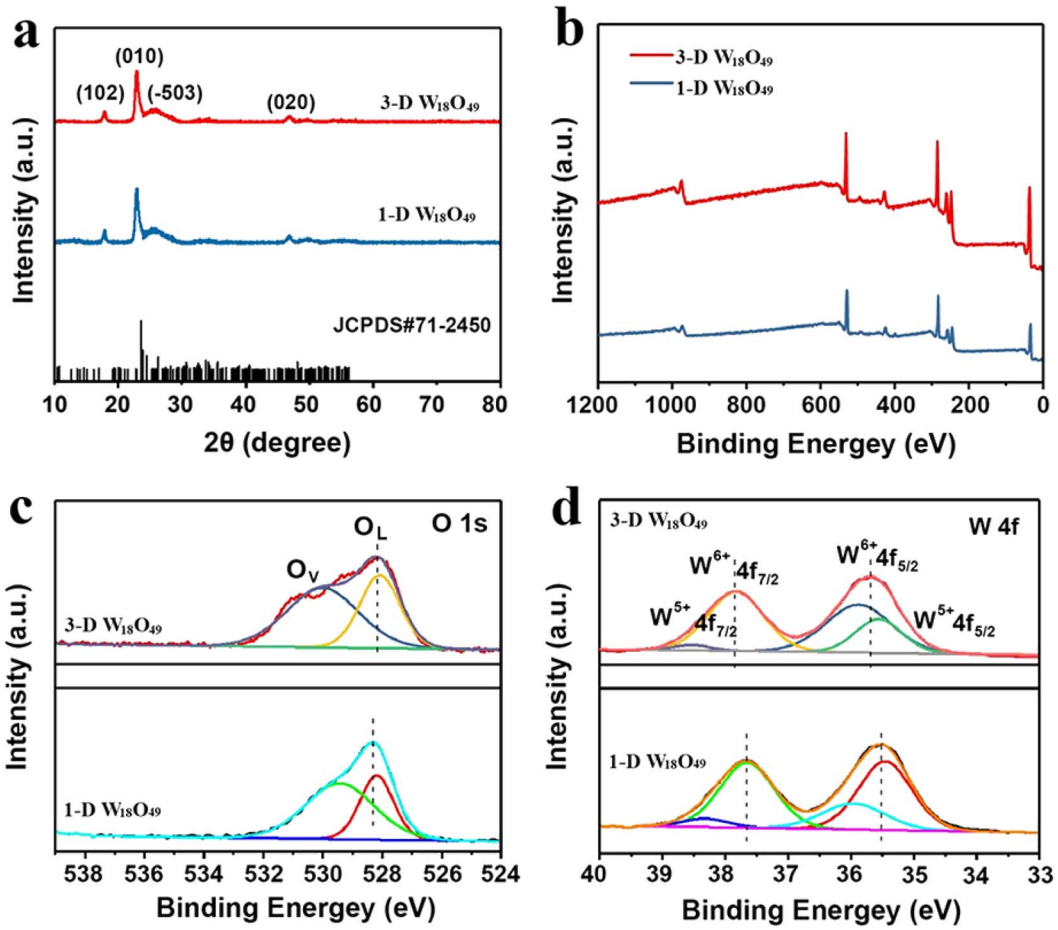

Fig. 3 (a) XRD patterns and (b) XPS spectra of 1-D $W_{18}O_{49}$ nanowires and 3-D urchin-like $W_{18}O_{49}$, and the corresponding high-resolution XPS spectra of (c) O 1s and (d) W 4f.

result was a direct proof of the existence of oxygen vacancies in 1-D and 3-D $W_{18}O_{49}$, and the oxygen vacancy ratio of 3-D $W_{18}O_{49}$ was significantly higher than that of 1-D $W_{18}O_{49}$. Additionally, since the EPR spectroscopy is also a highly effective characterization for the detection surface oxygen vacancies of prepared two photo-catalysts. And we could conclude that the oxygen vacancy in 3-D $W_{18}O_{49}$ was more abundant than 1-D $W_{18}O_{49}$ from the EPR signals in Fig. S3,† which was consistent with above XPS results in Fig. 3c. Moreover, two different valence states of W element (namely W^{6+}, W^{5+}) corresponding to $W4f_{5/2}$ and $W4f_{7/2}$ could be observed in the W4f high-resolution XPS spectrum (Fig. 3d). For 3-D $W_{18}O_{49}$, the peaks at 35.70 and 38.50 eV were rated to $W4f_{7/2}$ and $W4f_{5/2}$ characteristic peaks of W^{6+}, respectively. The second double peak with binding energies of 34.91 and 37.10 eV were attributed to the $W4f_{7/2}$ and $W4f_{5/2}$ characteristic peaks of W^{5+}. The emergence of the low valence state W^{5+} was attributed to the short W–W distances (0.26 nm) and the removal of oxygen occurs at the shear planes, which could further verify the existence of a large number of oxygen vacancies.[41,42] In addition, the binding energy of W 4f for 1-D $W_{18}O_{49}$ shifts by 0.2 eV toward lower value than that of the 3-D $W_{18}O_{49}$, which was attributed to the existence of larger oxygen vacancies in 3-D $W_{18}O_{49}$. The oxygen vacancies and W^{5+} defects could provide more active sites and would have important influence on the photocatalytic properties of as-prepared $W_{18}O_{49}$. To better study the photocatalytic properties and compare their differences of two forms of $W_{18}O_{49}$, the optical properties and separation efficiency of both photo-catalysts were explored by a sequence of photoelectrochemical characterizations.

3.2 Optical properties of prepared catalysts

It is well known that the optical absorption efficiency plays a decisive role in determining of photocatalytic performance.[43] Herein, the light trapping properties of 1-D $W_{18}O_{49}$ nanowires and 3-D urchin-like $W_{18}O_{49}$ were analyzed by UV-Vis-NIR absorption spectrum, and the related information was shown in Fig. 4. Two different dimensional sizes of $W_{18}O_{49}$ particles both presented a large absorption throughout the visible and near-infrared regions, which could be attributed to the plasmon resonance absorption driven by the existence of lots of oxygen vacancies in $W_{18}O_{49}$. Among them, 3-D $W_{18}O_{49}$ had stronger responsiveness in the UV-Vis-NIR region than 1-D $W_{18}O_{49}$, and the relevant proof information was shown in Fig. 4a. We could ascribe this phenomenon to the existence of 3-D urchin-like hierarchical structure, which not only could provide large surface area (Fig. 2) but also facilitate the multiple light scattering between the radial nanorods.[44,45] Besides, the bandgap information of the as-prepared samples was further studied by the relevant Tauc plots of UV-Vis spectra, as shown in Fig. 4b. The band gap was calculated using the Kubelka–Munk eqn (1).[46]

$$\alpha h\nu = k(h\nu - E_g)^{n/2} \quad (1)$$

where α, h, ν and k represent the diffuse absorption coefficient, plank constant, light frequency and a constant, respectively. It was estimated that the band gap of 3-D $W_{18}O_{49}$ (3.35 eV) was lower than that of 1-D $W_{18}O_{49}$ nanowires (3.70 eV), which could be inferred from Fig. 4b. Therefore, the light absorption range of 3-D urchin-like $W_{18}O_{49}$ was extended and then the light utilization efficiency was improved, which was crucial to obtain a better photocatalytic performance.[23,47] In addition, the potential of the valence band (VB) of two $W_{18}O_{49}$ semiconductors was determined through the Mott–Schottky measurements.[48,49] And the relevant results were shown in the Fig. S4,† the VB value of 1-D $W_{18}O_{49}$ and 3-D $W_{18}O_{49}$ were evaluated to be about 3.16 eV and 3.01 eV, respectively. Mott–Schottky (MS) plot was employed to investigate the CB of 3-D $W_{18}O_{49}$.[50,51] As shown in Fig. S5,† an obvious positive slope for MS plot was observed, indicating 3-D $W_{18}O_{49}$ belonged to n-type semiconductors. In fact, the position of the CB is close to the flat potential of the n-type semiconductors. The flat potential of 3-D $W_{18}O_{49}$ was further determined to be −0.54 eV (*vs.* Ag/AgCl at pH 7). The corresponding CB of 3-D $W_{18}O_{49}$ was converted to be about −0.34 eV (*vs.* NHE) according to the eqn (2). Based on the eqn (3), the VB of 3-D $W_{18}O_{49}$ was calculated to be +3.01 eV.

$$E_{NHE} = E_{Ag/AgCl} + 0.197 \quad (2)$$

$$E_g = E_{VB\text{-}ECB} \quad (3)$$

3.3 The separation efficiency of photogenerated charge carriers

To comprehensively investigate the separation and transfer efficiency of photo-excited charges over the photo-catalysts, the PL, time-resolved PL (TRPL) and EIS of the samples were carried out, and the detailed characterization results were presented in Fig. 5. Firstly, as shown in Fig. 5a, the fluorescence signal of 3-D urchin-like $W_{18}O_{49}$ was lower than that of $W_{18}O_{49}$ nanowires, which indicated that the 3-D $W_{18}O_{49}$ had more efficient charge separation efficiency. Furthermore, the TRPL was been demonstrated to be an effective tool for studying the dynamics of specific charge carrier, and the relevant TRPL results of 1-D $W_{18}O_{49}$ and 3-D $W_{18}O_{49}$ were shown in the Fig. 5b. It was obvious that the average lifetime value of 3-D $W_{18}O_{49}$ (20.23 ns) was longer than that of the 1-D $W_{18}O_{49}$ (5.45 ns), indicating that the 3-D $W_{18}O_{49}$ particle could appear larger defects, which had also been verified by the EPR technique (Fig. S1†). Generally, the higher photocurrent value also stands for more photogenerated electrons and higher separation efficiency. When the light source was switched on and off at 20 second intervals, the photocurrent signals could show vigorous spikes and decreases. Notably, the 3-D $W_{18}O_{49}$ had a higher signal (Fig. 5c) under the light illumination, which corresponded to higher light trapping and lower photogenerated charge recombination efficiency. To better explain above research results, there were differences in electron transfer efficiency between the two as-prepared catalysts. And the EIS was used to explore the real reason. As shown in Fig. 5d, the 3-D $W_{18}O_{49}$ photocatalyst possessed smaller radius, which further implied 3-D $W_{18}O_{49}$ had lower charge transfer impedance and higher charge separation efficiency in comparison with 1-D $W_{18}O_{49}$.

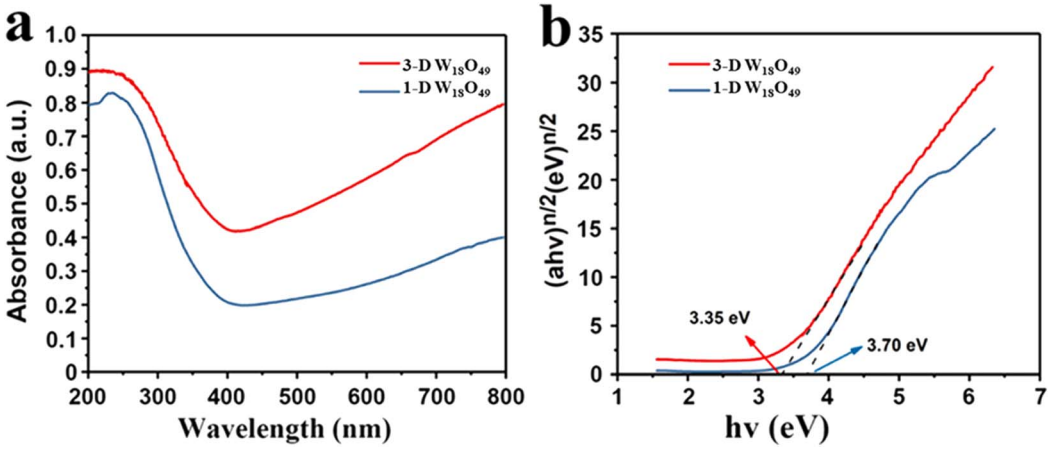

Fig. 4 (a) The UV-Vis diffuse absorbance spectra and (b) the corresponding plots of $(\alpha h\nu)^{n/2}$ *vs.* photoenergy ($h\nu$) of 1-D $W_{18}O_{49}$ nanowires and 3-D urchin-like $W_{18}O_{49}$.

3.4 Photocatalytic activity of the prepared photocatalysts

As shown above, the morphological difference of $W_{18}O_{49}$ particles brought about the difference in the surface area (Fig. 2), light absorption (Fig. 4) and separation efficiency of photogenerated charge (Fig. 5). These properties were important factors that could determine the photocatalytic performance of the photocatalysts.[52,53]

Herein, the degradation behavior of MB was taken as a typical example to investigate the specific photocatalytic

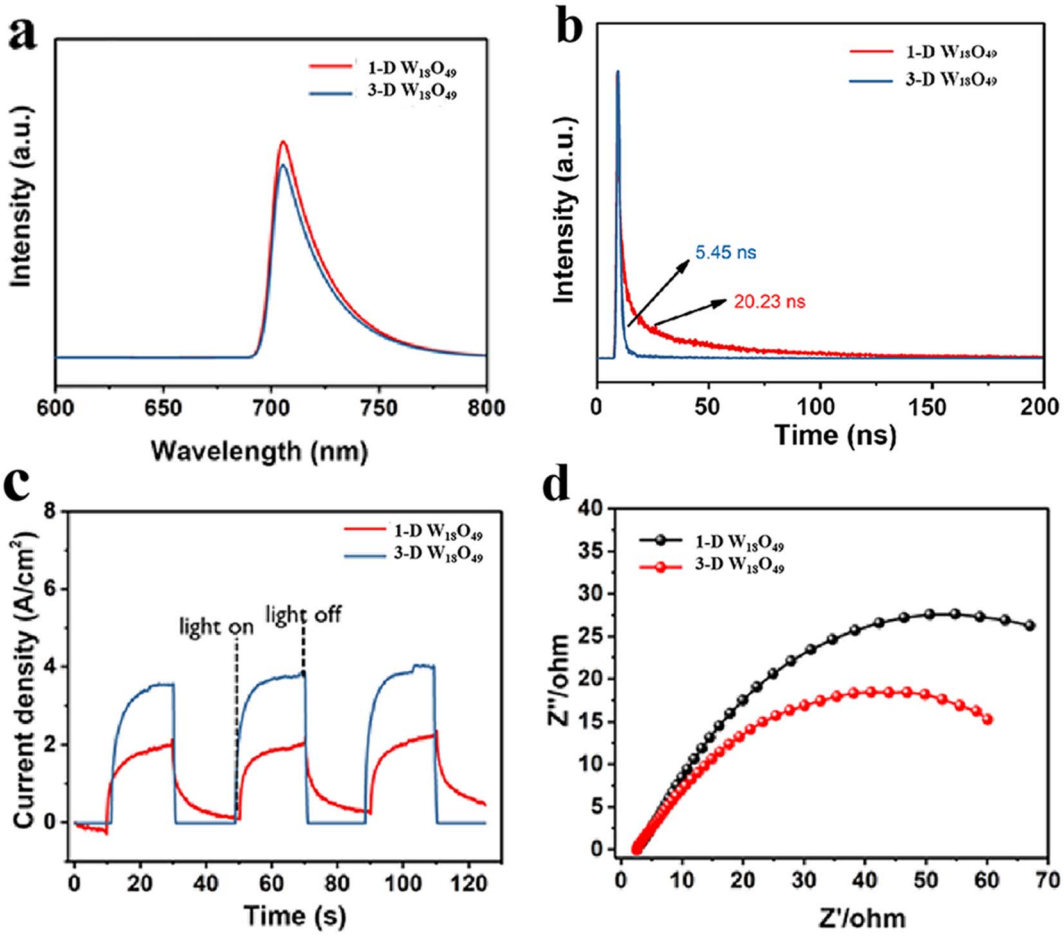

Fig. 5 (a) Photoluminescence spectra, (b) time-resolved transient PL decay (c) photocurrent transient responses and (d) electrochemical impedance spectra of 1-D $W_{18}O_{49}$ nanowires and 3-D urchin-like $W_{18}O_{49}$.

activity of 1-D $W_{18}O_{49}$ nanowires and 3-D urchin-like $W_{18}O_{49}$, the corresponding degradation activities and mechanism were shown in the Fig. 6. The dye concentration remained same under all experimental conditions. To exclude the effect of adsorption on the reduction of MB, the MB solution was exposed to dark conditions for 20 minutes. As shown in Fig. 6a, the MB content was not reduced in the dark, which indicated that the reduction of MB content in the system was only related to the photodegradation of the photocatalyst. In addition, the MB solution containing the two catalysts was irradiated for 120 minutes to compare the photocatalytic degradation rate of MB by the two catalysts. When $W_{18}O_{49}$ nanowires was used in the photocatalytic system, the concentration of MB decreased by 45% within 120 minutes, and 70% MB had been degraded in 120 min when 3D urchin-like $W_{18}O_{49}$ was employed. According to following eqn (4),[54] the values of photocatalytic reaction rates of 1-D $W_{18}O_{49}$ nanowires and 3-D urchin-like $W_{18}O_{49}$ were measured to be 0.00312 min^{-1} and 0.00932 min^{-1} respectively, as shown in Fig. 5b.

$$\ln(C_0/C_t) = kt \quad (4)$$

where k is the apparent rate constant, t is the reaction time, C_t is the concentration at irradiation time t, C_0 is the initial concentration. Furthermore, the time dependent absorption spectra of MB dye in the presence of 1-D $W_{18}O_{49}$ and 3-D $W_{18}O_{49}$ photocatalysts were shown separately in the Fig. 6c and d. The MB dye showed strong characteristic absorption peak at 670 nm and shoulder peak at 616 nm.[55] The results showed that the absorption maximum had a steady decline trend within 120 minutes no matter what kind of nanomaterials existed, however, the reduction rate of MB in 3-D urchin-like $W_{18}O_{49}$ catalysis was much faster than that in 1-D $W_{18}O_{49}$ nanowires. As discussed above, the 3-D $W_{18}O_{49}$ has been found to exhibit better catalytic performance and catalytic rate for the decomposition of MB than that of $W_{18}O_{49}$ nanowires. Furthermore, it was found that the morphology of the 3-D $W_{18}O_{49}$ particles did not change and still had a three-dimensional structure after the photocatalytic degradation of MB (Fig. S6†), which indicated

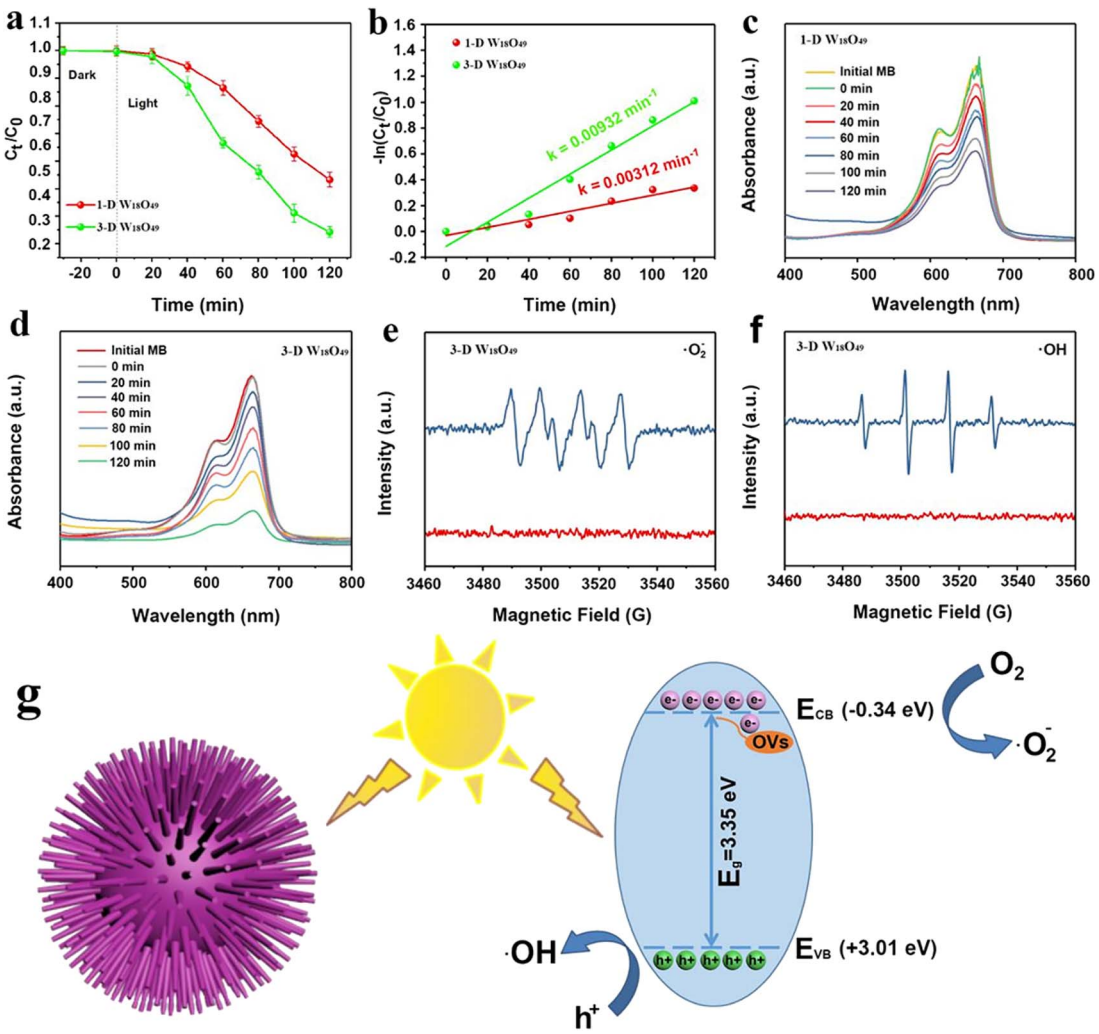

Fig. 6 (a) The photocatalytic degradation of methylene blue and (b) plot of ln C_t/C_0 *vs.* time under simulated solar irradiation over 1-D $W_{18}O_{49}$ nanowires and 3-D urchin-like $W_{18}O_{49}$, the UV-Vis spectral changes of methylene blue as a function of irradiation time in the presence of (c) 1-D $W_{18}O_{49}$ nanowires and (d) 3-D urchin-like $W_{18}O_{49}$, the EPR spectra of (e) $^{\bullet}O_2^-$ and (f) $^{\bullet}OH$ for 3-D urchin-like $W_{18}O_{49}$, and (g) the schematic illustration of the reaction mechanism involved in the photocatalytic activity of 3-D urchin-like $W_{18}O_{49}$.

that the particle was expected to achieve reuse in the field of photocatalytic degradation.

It is well known that the produced $^{\bullet}OH$ and $^{\bullet}O_2^-$ radicals had a major impact on the degradation efficiency. To better study the mechanism of 3-D urchin-like $W_{18}O_{49}$, the low-temperature ESR technology was carried to study the active radicals. It was obvious that the signal of $^{\bullet}O_2^-$ (Fig. 6e) could be observed in the 3-D urchin-like $W_{18}O_{49}$. Meanwhile, the $^{\bullet}OH$ signal (Fig. 6f) was also detected under the same conditions. Based on the above experimental results and discussions, we proposed a possible mechanism for the better photocatalytic performance of 3-D urchin-like $W_{18}O_{49}$ particle, as shown in Fig. 6g. The conduction band (CB) and valence band (VB) of 3-D urchin-like $W_{18}O_{49}$ were further determined. And the corresponding CB and VB of 3-D urchin-like $W_{18}O_{49}$ were estimated to be about −0.34 and +3.01 eV, respectively. The CB potential (−0.34 eV) of 3-D urchin-like $W_{18}O_{49}$ was more negative than that of E^{θ} ($^{\bullet}O_2^-/O_2$) (−0.33 eV), while the active species ($^{\bullet}O_2^-$) could be generated. Besides, and VB potential (+3.01 eV) of 3-D urchin-like $W_{18}O_{49}$ was more positive that of E^{θ} ($^{\bullet}OH/H_2O$) (+1.99 eV), the active species ($^{\bullet}OH$) might be formed, which was consistent with the ESR results. Under visible light excitation, a large number of photogenerated electrons and holes were produced on 3-D urchin-like $W_{18}O_{49}$. Photogenerated electrons on 3-D urchin-like $W_{18}O_{49}$ could capture O_2 and generate $^{\bullet}O_2^-$ due to more negative potential, while, holes could directly oxidize H_2O into $^{\bullet}OH$. Compared to the 1-D $W_{18}O_{49}$ nanowires, the unique three-dimensional hierarchical structure in 3-D $W_{18}O_{49}$ would be more effective in harvesting light through multiple scattering between the radial nanorods, which could generate more electrons and holes. Meanwhile, lots of electrons concentrated on the tip of the nanorods because of the tip effect, and therefore, 3-D $W_{18}O_{49}$ was more conducive to adsorption, activation and degradation of pollutants like MB. Then, the photo-induced electrons could interact with oxygen and water adsorbed on the surface to generate active radicals $^{\bullet}O_2^-$ and $^{\bullet}OH$, which could contribute to the degradation of MB.[56] Therefore, the larger surface area, more light absorption and higher effective charge separation brought by the unique 3-D urchin-like structure work synergistically, resulting in the excellent photocatalytic performance.

4 Conclusions

1-D $W_{18}O_{49}$ nanowire and 3-D urchin-like $W_{18}O_{49}$ particle were successfully synthesized under different reaction temperatures through the hydrothermal method. In addition, we systematically evaluated the differences in photocatalytic performance between these two particles. The comprehensive characterizations and control experiments indicted that the hierarchical urchin-like structure given 3-D $W_{18}O_{49}$ particle a larger BET surface areas (120 $m^2\ g^{-1}$) than 1-D $W_{18}O_{49}$ nanowires (75 $m^2\ g^{-1}$), which led to more excellent optical properties of 3-D urchin-like $W_{18}O_{49}$ particle: the larger light absorption capacity and light utilization efficiency; lower charge transfer impedance and complexation efficiency of photogenerated charges, and so on. Furthermore, the actual photocatalytic performance was measured by taking MB degradation as an example, the result was that the photocatalytic reaction rates of 3-D urchin-like $W_{18}O_{49}$ particles was about three times than that of 1-D $W_{18}O_{49}$ nanowires. This study is helpful for us to better understand the influence of morphology on the photocatalytic performance of $W_{18}O_{49}$ material, which is conducive to the better application of $W_{18}O_{49}$ or their composites in the field of photocatalysis.

Data availability

Juan Wang: investigation, methodology, writing-original draft, funding acquisition. Jin Ye: methodology, experimental characterization, writing-editing.

Conflicts of interest

The authors declare that they have no known competing financial interests or personal relationships that could have appeared to influence the work reported in this paper.

Acknowledgements

Financial support from the Talent Introduction Project (40621051).

References

1 X. Wang, X. Zhang, Y. Zhang, Y. Wang, S.-P. Sun, W. D. Wu and Z. Wu, Nanostructured Semiconductor Supported Iron Catalysts for Heterogeneous Photo-Fenton Oxidation: A Review, *J. Mater. Chem. A*, 2020, **8**(31), 15513–15546.

2 J. Ye, J. Xu, C. Li, D. Ti, X. Zhao, Q. Wang, W. Lv, J. Wang, H. Xie, Y. Li, Z. Liu and Y. Fu, Novel N-Black In_2O_3-x/$InVO_4$ Heterojunction for Efficient Photocatalytic Fixation: Synergistic Effect of Exposed (321) Facet and Oxygen Vacancy, *J. Mater. Chem. A*, 2021, **9**(43), 24600–24612.

3 D. Yun, E. Ayla, D. Bregante and D. Flaherty, Reactive Species and Reaction Pathways for the Oxidative Cleavage of 4-Octene and Oleic Acid with H_2O_2 over Tungsten Oxide Catalysts, *ACS Catal.*, 2021, **11**(593), 3137–3152.

4 Z. Jin, J. Li, D. Liu, Y. Sun, X. Li, Q. Cai, H. Ding and J. Gui, Effective Promotion of Spacial Charge Separation of Dual S-scheme (1D/2D/0D) WO_3@$ZnIn_2S_4$/Bi_2S_3 Heterojunctions for Enhanced Photocatalytic Performance under Visible Light, *Sep. Purif. Technol.*, 2022, **284**(2), 120207.

5 X. Xiao, T. Ding, L. Yuan, Y. Shen, Q. Zhong, X. Zhang, Y. Cao, B. Hu, T. Zhai, L. Gong, J. Chen, Y. Tong, J. Zhou and Z. Wang, WO_{3-x}/MoO_{3-x} Core/Shell Nanowires on Carbon Fabric as an Anode for All-Solid-State Asymmetric Supercapacitors, *Adv. Energy Mater.*, 2012, **2**(11), 1328–1332.

6 C. Valentin, F. Wang and G. Pacchioni, Tungsten Oxide in Catalysis and Photocatalysis: Hints from DFT, *Top. Catal.*, 2013, **56**(15–17), 1404–1419.

7 J. Liang, J. Yu, W. Xing, W. Tang, N. Tang and J. Guo, 3D interconnected Network Architectures Assembled from $W_{18}O_{49}$ and Ti_3C_2 MXene with Excellent Electrochemical

Properties and CDI Performance, *Chem. Eng. J.*, 2022, **435**, 134922.

8 L. Han, J. Xia, X. Hai, Y. Shu, X. Chen and J. Wang, Protein-Stabilized Gadolinium Oxide-Gold Nanoclusters Hybrid for Multimodal Imaging and Drug Delivery, *ACS Appl. Mater. Interfaces*, 2017, **9**(8), 6941–6949.

9 Z. Wang, M. Hu and Y. Qin, Solvothermal Synthesis of WO_3 Nanocrystals with Nanosheet and Nanorod Morphologies and the Gas-Sensing Properties, *Mater. Lett.*, 2016, **171**, 146–149.

10 C. Balázsi, L. Wang, E. Zayim, I. Szilágyi, K. Sedlacková, J. Pfeifer, A. Tóth and P. Gouma, Nanosize Hexagonal Tungsten Oxide for Gas Sensing Applications, *J. Eur. Ceram. Soc.*, 2008, **28**(5), 913–917.

11 A. Aral and J. Gardeniers, Synthesis and Atmospheric Pressure Field Emission Operation of $W_{18}O_{49}$ Nanorods, *J. Phys. Chem. C*, 2008, **112**(39), 15183–15189.

12 C. Guo, S. Yin, Y. Huang, Q. Dong and T. Sato, Synthesis of $W_{18}O_{49}$ Nanorod via Ammonium Tungsten Oxide and Its Interesting Optical Properties, *Langmuir*, 2011, **27**(19), 12172–12178.

13 B. Bishal, B. Paul, S. S. Dhar and S. Vadivel, Facile Hydrothermal Synthesis of Ultrasmall $W_{18}O_{49}$ Nanoparticles and Studies of Their Photocatalytic Activity towards Degradation of Methylene Blue, *Mater. Chem. Phys.*, 2017, **188**, 1–7.

14 N. Meng, B. Jin, C. Chow and C. Saint, Recent Developments in Photocatalytic Water Treatment Technology: A Review, *Water Res.*, 2010, **44**(10), 2997–3027.

15 S. Mei, M. Pan, J. Wang, X. Zhang, S. Song, C. Li and G. Liu, Self-assembly of Strawberry-like Organic-inorganic Hybrid Particle Clusters with Directionally Distributed Bimetal and Facile Transformation of the Core and Corona, *Polym. Chem.*, 2020, **11**(18), 3136–3151.

16 J. Wang, M. Pan, J. Yuan, Q. Lin, X. Zhang, G. Liu and L. Zhu, Hollow Mesoporous Silica with Hierarchical Shell from in-situ Synergetic Soft-Hard Double Templates, *Nanoscale*, 2020, **12**(19), 10863–10871.

17 Y. Fu, K. Zhang, Y. Zhang, Y. Cong and Q. Wang, Fabrication of Visible-light-active MR/NH_2-MIL-125(Ti) Homojunction with Boosted Photocatalytic Performance, *Chem. Eng. J.*, 2021, **412**, 128722.

18 J. Guo, D. Ma, F. Sun, G. Zhuang, Q. Wang, A. Al-Enizi, A. Nafady and S. Ma, Substituent Engineering in g-C_3N_4/COF Heterojunctions for Rapid Charge Separation and High Photo-redox Activity, *Sci. China: Chem.*, 2022, **65**(9), 1704–1709.

19 K. G. Bhattacharyya and A. Sharma, Kinetics and Thermodynamics of Methylene Blue Adsorption on Neem (Azadirachta Indica) Leaf Powder, *Dyes Pigm.*, 2005, **65**(1), 51–59.

20 J. Galvan, M. X. Borsoi, L. Julek, D. Bordin and F. B. T. Alves, Methylene Blue for the Treatment of Health Conditions: a Scoping Review, *Braz. Arch. Biol. Technol.*, 2021, **64**(4), e21200266.

21 W. Lü, Y. Wu, J. Chen and Y. Yang, Facile Preparation of Graphene-Fe_3O_4 Nanocomposites for Extraction of Dye from Aqueous Solution, *CrystEngComm*, 2014, **16**, 609–615.

22 E. Cserhati, E. Forgacs and G. Oros, Removal of Synthetic Dyes from Wastewater: A Review, *Environ. Int.*, 2004, **30**, 953–971.

23 R. A. Pereira, A. F. Salvador, P. Dias and M. F. R. Pereira, Perspectives on Carbon Materials as Powerful Catalysts in Continuous Anaerobic Bioreactors, *Water Res.*, 2016, **101**(15), 441–447.

24 N. Abdullah, M. Mohamed, N. Shohaimi, A. Lazim, A. Halim, N. Shukri and M. Razab, Enhancing the Decolorization of Methylene Blue Using a Low-Cost Super-Absorbent Aided by Response Surface Methodology, *Molecules*, 2021, **26**(15), 4430.

25 G. Zheng, Y. Cui, Y. Zhou, Z. Jiang, Q. Wang, M. Zhou, P. Wang and Y. Yu, Photoenzymatic Activity of Artificial-Natural Bienzyme Applied in Biodegradation of Methylene Blue and Accelerating Polymerization of Dopamine, *ACS Appl. Mater. Interfaces*, 2021, **13**(47), 56191–56204.

26 M. Xu, S. Ma, J. Li and M. Yuan, Multifunctional 3D Polydimethylsiloxane Modified MoS_2@biomass-Derived Carbon Composite for Oil/Water Separation and Organic Dye Adsorption/Photocatalysis, *Colloids Surf., A*, 2022, **637**, 128281.

27 C. Muthukemar, S. Alam, E. lype and K. Prakash, Statistical Analysis of Photodegradation of Methylene Blue Dye under Natural Sunlight, *Opt. Mater.*, 2021, **122**(8), 111809.

28 L. Bi, Z. Chen, L. Li, J. Kang and J. Shen, Selective Adsorption and Enhanced Photodegradation of Diclofenac in Water by Molecularly Imprinted TiO_2, *J. Hazard. Mater.*, 2021, **407**(5), 124759.

29 W. Ma, Y. Li, M. Zhang, S. Gao and G. Fu, Biomimetic Durable Multifunctional Self-Cleaning Nanofibrous Membrane with Outstanding Oil/Water Separation, Photodegradation of Organic Contaminants, and Antibacterial Performances, *ACS Appl. Mater. Interfaces*, 2020, **12**(31), 34999–35010.

30 C. Wang, Y. Lei, Q. Lv, W. Kong, F. Wan and W. Chen, Abundant Oxygen Vacancies Promote Bond Breaking of Hydrogen Peroxide on 3d Urchin-Like Pd/$W_{18}O_{49}$ Surface to Achieve High-Performance Catalysis of Hydroquinone Oxidation, *Appl. Catal., B*, 2022, **315**, 121547.

31 H. Zhang, Y. Wang, S. Zuo, W. Zhou, J. Zhang and X. Lou, Isolated Cobalt Centers on $W_{18}O_{49}$ Nanowires Perform as a Reaction Switch for Efficient CO_2 Photoreduction, *J. Am. Chem. Soc.*, 2021, **143**(5), 2173–2177.

32 Y. Li, W. Chen, Z. Liu, D. Cao, Y. Chen, K. Thummavichai, N. Wang and Y. Zhu, In situ Fabrication of Porous Biochar Reinforced $W_{18}O_{49}$ Nanocomposite for Methylene Blue Photodegradation, *RSC Adv.*, 2022, **12**, 14902–14911.

33 M. Li, S. Zhang, M. Alwafi, J. Han and H. Wang, Multiple Light Scattering and Nanotip Effect of Hierarchical Sea Urchin-like $W_{18}O_{49}$ Boosting Photocatalytic Hydrolysis of Ammonia Borane, *Int. J. Hydrogen Energy*, 2021, **46**(36), 18964–18976.

34 N. Zhang, Y. Zhao, Y. Lu and G. Zhu, Preparation of Aligned $W_{18}O_{49}$ Nanowire Clusters with High Photocatalytic Activity, *Mater. Sci. Eng., B*, 2017, **218**, 51–58.

35 G. Xi, S. Ouyang, P. Li, J. Ye, Q. Ma, N. Su, H. Bai and C. Wang, Ultrathin $W_{18}O_{49}$ Nanowires with Diameters below 1 nm: Synthesis, Near-Infrared Absorption, Photoluminescence, and Photochemical Reduction of Carbon Dioxide, *Angew. Chem., Int. Ed.*, 2012, **51**(10), 2395–2399.

36 S. Park, H.-W. Shim, C. W. Lee, H. J. Song, J.-C. Kim and D.-W. Kim, High-power and Long-life Supercapacitive Performance of Hierarchical, 3-D Urchin-like $W_{18}O_{49}$ Nanostructure Electrodes, *Nano Res.*, 2016, **9**, 633–643.

37 J. Polleux, N. Pinna, M. Antonietti and M. Niederberger, Growth and Assembly of Crystalline Tungsten Oxide Nanostructures Assisted by Bioligation, *J. Am. Chem. Soc.*, 2005, **127**, 15595–15601.

38 Z. Chen, Q. Wang, H. Wang, L. Zhang and G. Song, Ultrathin PEGylated $W_{18}O_{49}$ Nanowires as a New 980nm-Laser-Driven Photothermal Agent for Efficient Ablation of Cancer Cells In Vivo, *Adv. Mater.*, 2013, **25**(14), 2095–2100.

39 C. Chen, T. Jiang, J. Hou, T. Zhang, G. Zhang, Y. Zhang and X. Wang, Oxygen Vacancies induced Narrow Band Gap of BiOCl for Efficient Visible-light Catalytic Performance from Double Radicals, *J. Mater. Sci. Technol.*, 2022, **114**, 240–248.

40 T. Xiong, Y. Zhang, W. S. V. Lee and J. Xue, Defect Engineering in Manganese-Based Oxides for Aqueous Rechargeable Zinc-Ion Batteries: A Review, *Adv. Energy Mater.*, 2020, **10**, 2001769.

41 P. Chen, M. Qin, D. Zhang, Z. Chen, B. Jia, Q. Wan, H. Wu and X. Qu, Combustion Synthesis and Excellent Photocatalytic Degradation Properties of $W_{18}O_{49}$, *CrystEngComm*, 2015, **39**(2), 1196–1201.

42 S. Park, H.-W. Shim, C. W. Lee, H. J. Song, J.-C. Kim and D.-W. Kim, High-power and Long-life Supercapacitive Performance of Hierarchical, 3-D Urchin-Like $W_{18}O_{49}$ Nanostructure Electrodes, *Nano Res.*, 2016, **9**(3), 633–643.

43 H. Bai, N. Su, W. Li, X. Zhang, Y. Yan, P. Li, S. Quyang, J. Ye and G. Xi, $W_{18}O_{49}$ Nanowire Networks for Catalyzed Dehydration of Isopropyl Alcohol to Propylene under Visible Light, *J. Mater. Chem. A*, 2013, **1**(20), 6125–6129.

44 Y. Liu, Z. Zhang, Y. Fang, B. Liu, J. Huang, F. Miao, Y. Bao and B. Dong, IR-Driven Strong Plasmonic-Coupling on Ag Nanorices/$W_{18}O_{49}$ Nanowires Heterostructures for Photo/Thermal Synergistic Enhancement of H_2 Evolution from Ammonia Borane, *Appl. Catal., B*, 2019, **252**, 164–173.

45 W. Ren, H. Zhang, D. Kong, B. Liu, Y. Yang and C. Cheng, A Three-dimensional Hierarchical TiO_2 Urchin as a Photoelectrochemical Anode with Omnidirectional Anti-Reflectance Properties, *Phys. Chem. Chem. Phys.*, 2014, **16**, 22953–22957.

46 G. Eshaq, S. Wang, H. Sun and M. Sillanpää, Core/shell $FeVO_4$@BiOCl Heterojunction as a Durable Heterogeneous Fenton Catalyst for the Efficient Sonophotocatalytic Degradation of P-nitrophenol, *Sep. Purif. Technol.*, 2020, **16**(231), 115915.

47 K. Mori, K. Miyawaki and H. Yamashita, Ru and Ru-Ni Nanoparticles on TiO_2 Support as Extremely Active Catalysts for Hydrogen Production from Ammonia-Borane, *ACS Catal.*, 2016, **6**(5), 3128–3135.

48 H. Liang, A. Acharjya, D. Anito, S. Vogl and B. Han, Rhenium-Metalated Polypyridine-Based Porous Polycarbazoles for Visible-Light CO_2 Photoreduction, *ACS Catal.*, 2019, **9**(5), 3959–3968.

49 H. Xu, J. Hu, D. Wang, Z. Li, Q. Zhang, Y. Luo, S.-H. Yu and H.-L. Jiang, Visible-Light Photoreduction of CO_2 in a Metal-Organic Framework: Boosting Electron-Hole Separation via Electron Trap States, *J. Am. Chem. Soc.*, 2015, **137**(42), 151004174149004.

50 Y. Fu, M. Tan, Z. Guo, D. Hao, Y. Xu, H. Du, C. Zhang, J. Guo, Q. Li and Q. Wang, Fabrication of Wide-spectra-responsive NA/NH_2-MIL-125(Ti) with Boosted Activity for Cr(VI) Reduction and Antibacterial Effects, *Chem. Eng. J.*, 2023, **452**, 139417.

51 S. Zheng, H. Du, L. Yang, M. Tan, N. Li, Y. Fu, D. Hao and Q. Wang, PDINH bridged NH_2-UiO-66(Zr) Z-scheme Heterojunction for Promoted Photocatalytic Cr(VI) Reduction and Antibacterial Activity, *J. Hazard. Mater.*, 2023, **447**, 130849.

52 S. Thirumalairajan, K. Girija, V. Mastelaro and N. Ponpandian, Photocatalytic Degradation of Organic Dyes under Visible Light Irradiation by Floral-like $LaFeO_3$ Nanostructures Comprised of Nanosheet Petals, *New J. Chem.*, 2014, **38**(11), 5480–5490.

53 J. Chen, J. Liu, S. Qiao, R. Xu and X. Lou, Formation of Large 2D Nanosheets via PVP-assisted Assembly of Anatase TiO_2 Nanomosaics, *Chem. Commun.*, 2011, **47**(37), 10443–10445.

54 J. Wang and T. Nonami, Photocatalytic Activity for Methylene Blue Decomposition of $NaInO_2$ with a Layered Structure, *J. Mater. Sci.*, 2004, **39**(20), 6367–6370.

55 Y. Zhao, Y. Wang, E. Liu, J. Fan and X. Hu, Bi2WO6 Nanoflowers: An Efficient Visible Light Photocatalytic Activity for Ceftriaxone Sodium Degradation, *Appl. Surf. Sci.*, 2018, **436**, 854–864.

56 B. Bhuyan, B. Paul, S. S. Dhar and S. Vadivel, Facile Hydrothermal Synthesis of Ultrasmall $W_{18}O_{49}$ Nanoparticles and Studies of Their Photocatalytic Activity towards Degradation of Methylene Blue, *Mater. Chem. Phys.*, 2017, **188**, 1–7.